

Microfluidic Overhauser DNP Chip for Signal-enhanced Compact NMR

Sebastian Kiss

Karlsruhe Institute of Technology

Neil MacKinnon

Karlsruhe Institute of Technology

Jan Korvink (✉ jan.korvink@kit.edu)

Institute 4 of Microstructure Technology, Karlsruhe Institute of Technology, Hermann-von-Helmholtz-Platz 1, 76344, Eggenstein-Leopoldshafen, Germany

Research Article

Keywords: Nuclear magnetic resonance, insensitive spectroscopic technique, situ dynamic nuclear polarisation

Posted Date: December 11th, 2020

DOI: <https://doi.org/10.21203/rs.3.rs-124072/v1>

License: © ⓘ This work is licensed under a Creative Commons Attribution 4.0 International License.

[Read Full License](#)

Version of Record: A version of this preprint was published at Scientific Reports on February 25th, 2021. See the published version at <https://doi.org/10.1038/s41598-021-83625-y>.

1 Microfluidic Overhauser DNP chip for 2 signal-enhanced compact NMR

3 Sebastian Z. Kiss¹, Neil MacKinnon¹, and J. G. Korvink^{1,*}

4 ¹Institute of Microstructure Technology, Karlsruhe Institute of Technology, Hermann-von-Helmholtz-Platz 1, 76344,
5 Eggenstein-Leopoldshafen, Germany

6 *jan.korvink@kit.edu

7 ABSTRACT

8 Nuclear magnetic resonance at low field strength is an insensitive spectroscopic technique, precluding portable applications with small sample volumes, such as needed for biomarker detection in body fluids. Here we report a compact double resonant chip stack system that implements *in situ* dynamic nuclear polarisation of a 130 nL sample volume, achieving a signal enhancement of 54 w.r.t. the thermal equilibrium level at a microwave power level of 0.5 W. This work overcomes instrumental barriers to the use of NMR detection for point-of-care applications.

9 Please note: Abbreviations should be introduced at the first mention in the main text – no abbreviations lists. Suggested
10 structure of main text (not enforced) is provided below.

11 Introduction

12 Significant research effort has been invested in recent years to achieve nuclear magnetic resonance (NMR) systems possessing
13 small form factors¹. Compact NMR systems based on permanent magnets offer attractive opportunities, including a significant
14 reduction in size and cost for hardware, and adaptable system operations, when compared to state-of-the-art high field
15 NMR spectrometers based on superconducting electromagnets². Only recently, technological progress has culminated in
16 commercially available compact systems for NMR spectroscopy, based on permanent magnets, which provide sufficient
17 performance for a variety of NMR and magnetic resonance imaging (MRI) applications. Micro NMR systems based on
18 CMOS integrated circuits^{3–6} as well as advances in micro-fabrication and lab-on-a-chip technologies^{7,8} are further advancing
19 miniaturisation, ultimately evolving towards handheld systems suitable for point-of-care and personalised diagnosis. Particularly,
20 microfabricated NMR probes^{9–17} can provide the efficient analysis of volume limited samples and even co-integrate new
21 functionalities to enable novel analytic approaches, such as NMR *in situ* electrochemistry.

22 However, the benefits stand in opposition to the technological challenges associated with the system integration of, e.g., the
23 sample container, the radio frequency (RF) coil, and the NMR transceiver. Importantly, the benefits of compact permanent
24 magnets come at the price of low magnetic field strengths (less than 2 T for NdFeB magnets), resulting in low NMR signal
25 sensitivity and poor B_0 -field homogeneity, as well as thermally and mechanically induced B_0 -field drift.

26 Overcoming these limitations, to enable high chemical shift resolution (< 0.01 ppm) NMR spectroscopy in a compact
27 format, is challenging and the subject of ongoing research. Efforts to address the issues related to the magnet include: design
28 optimisation of the magnet topology^{18–23}, the implementation of passive shims²⁴ and active electric shim coils^{25–28}, and
29 frequency/field locks for B_0 -field correction and stabilisation.

30 With this contribution we specifically address the lack of low field sensitivity, by employing out-of-equilibrium polarisation
31 enhancement of liquid state nuclear spins. Dynamic nuclear polarisation (DNP) is a strongly hyperpolarising effect that was
32 first predicted by Albert Overhauser²⁹ and soon afterwards confirmed by Charles Schlichter and his team³⁰, but, despite its
33 advantages, is still not generally available. By miniaturising the DNP detection system, the opportunities offered by increased
34 portability stand in contrast to numerous instrumental challenges that must be overcome. Inhomogeneities in low weight
35 low field magnets result in significantly broadened NMR linewidths. Microwave and radiofrequency signals for DNP differ
36 considerably in wavelength, making double resonance hard to achieve in an overlapping sample volume. Remanent microwave
37 electric field components lead to rapid sample heating due to water absorption. Microwave equipment with a miniaturised
38 footprint delivers insufficient power output for typical sample volumes.

39 The existing literature focuses on conventional fabrication technologies and sample volumes of several microlitres to
40 millilitres. For example, Armstrong and co-workers³¹, presented a portable X-band (9.5 GHz) system for solution state ODNP
41 based on a 0.35 T Halbach permanent magnet. A home built NMR double U-coil was implemented into a modified commercial

42 TE₁₀₂ X-band MW cavity resonator, which was loaded by a capillary containing 4 μ L of sample. Münnemann et al.³², reported
 43 on a mobile DNP polariser based on a 0.3 T permanent magnet for clinical applications. The field-tunable Halbach magnet
 44 weighs 90 kg and is equipped with a commercial ENDOR probe head featuring a dielectric MW resonator, accepting 3 mm
 45 sample tubes. Garcia and co-workers³³ presented an L-band (1.1 GHz) loop-gap MW resonator inside a solenoid NMR detection
 46 coil, for ODNP ¹H experiments on water dynamics employing a 0.04 T permanent magnet of Halbach design and 8 mm NMR
 47 tubes. For a comparative study of ¹H and ¹⁹F ODNP in fluorinated benzenes, Neudert et al.³⁴, employed a nitrogen gas cooled,
 48 commercially available electron nuclear double resonance (ENDOR) probe head for operation at 9.69 GHz inside a 0.345 T
 49 home-built permanent magnet array³⁵. The authors used sealed glass tubes, filled with approximately 13 μ L of sample. Keller
 50 et al.³⁶ recently demonstrated chemically resolved ¹H NMR ODNP operating at 0.35 T using a home-built dielectric resonator,
 51 accommodating a sample capillary with 1 mm diameter. This was possible by including field shimming coils, permitting 4 Hz
 52 spectral resolution. Übrück et al.³⁷ recently described a benchtop ODNP system based on a home-built C-shaped permanent
 53 magnet at 0.342 T (15 kg) and commercial dielectric EPR resonator, compatible with 1 mm sample capillaries. With this system,
 54 the authors also demonstrated ¹H chemical shift resolution by shimming through adjustment of the unit permanent magnet
 55 positions.

56 Inspired by the work of Johansson et al.³⁸ and Narkowicz and co-workers³⁹, this work aims to explore the feasibility of
 57 microfabricated, 14 GHz transmission line MW resonators for ODNP experiments. We report on an NMR probe head enabling
 58 *in situ* Overhauser DNP-enhanced NMR spectroscopy of nanoliter-sized liquid samples for analyses inside a compact, light
 59 weight and hence portable 0.5 T permanent magnet. The approximately 3.5 mm long and 411 μ m wide $\lambda/2$ -stripline resonator
 60 is integrated into a microfluidic chip and interacts with a sample volume of approximately 130 nL. Miniaturised, distributed
 61 resonators feature large power-to-field conversion efficiencies Λ and high filling factors, beneficial for experiments on volume
 62 limited samples. The following section on the system design summarises the challenges and potentials involved with the design
 63 of the double resonant ODNP probe head. In particular, we also describe our MEMS-based approach to co-integrate a MW
 64 resonator into a microfluidic chip, including the implementation of the electrical shims and an RF transceive coil. We then
 65 demonstrate the performance of our probe head by performing ¹H ODNP-enhanced NMR experiments and discuss benefits and
 66 disadvantages of the proposed concept. To the best of our knowledge, this is the first report on a compact microfabricated MW
 67 resonator integrated into a permanent magnet ODNP setup.

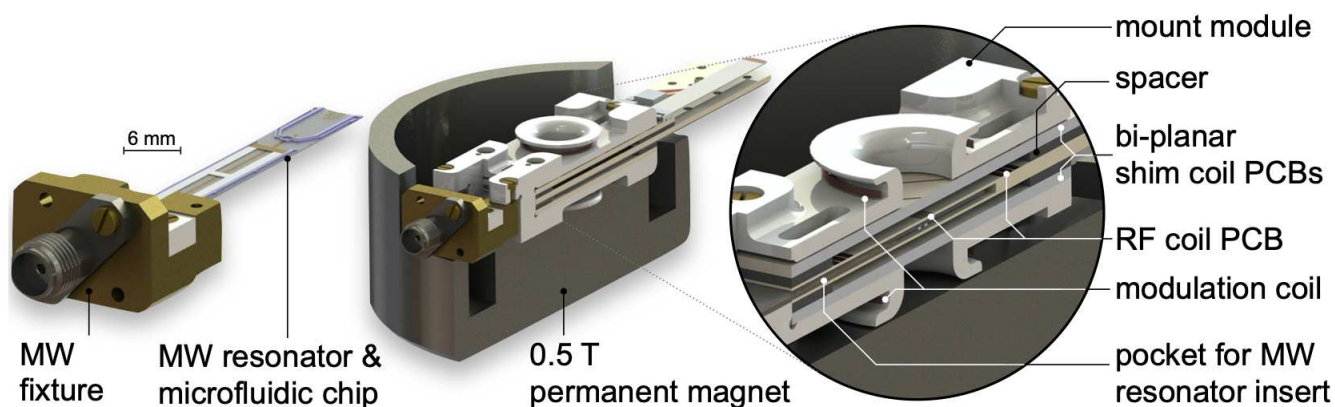


Figure 1. CAD views of the ODNP probe inside a palm-sized permanent magnet. The microfluidic chip features a sample reservoir and a MW resonator. A stacked figure-8 type RF transceive coil accepts the sample container and is sandwiched between a set of bi-planar electrical shim coils. A B_0 -field modulation coil is part of phase sensitive EPR detection. Figure used with permission⁴⁰.

68 Results

69 Resonator characterisation

70 For electrical characterisation, the resonator chips were mounted into the MW fixture as shown in Figure 6 (b), which was
 71 connected to a calibrated network analyser (N5224A, Agilent Technologies, Inc., USA) via a 50 Ω coaxial cable. Figure S3
 72 shows characteristic features of the presented double resonant ODNP probe head, such as the frequency tuning capability, or
 73 the typical shift in MW resonance frequency $\Delta f_L \approx -300$ MHz upon sample loading (panel b, top). The sample's Larmor
 74 frequencies are determined in value by the B_0 -field of the 0.5 T permanent magnet, which can only be marginally tuned via its
 75 built-in drift compensation coil, so that the ability to tune the MW resonator's resonance frequency is of particular importance

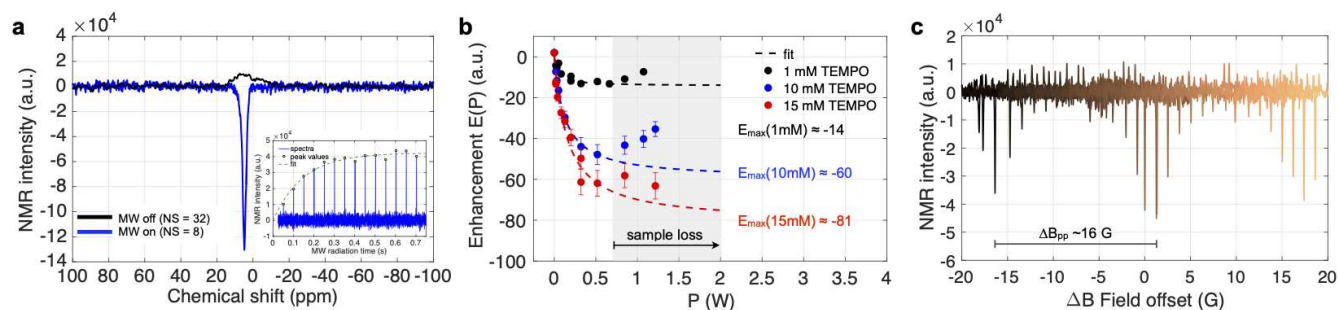


Figure 2. (a) Comparison between a thermal (32 scans) and the ODNP enhanced (8 scans) ^1H spectrum (130 nL of 10 mM TEMPOL in DI water, $P_{\text{MW}} \approx 0.52$ W). The inset illustrates the build up of the ODNP signal as a function of MW radiation time (see text for details). (b) Measured ^1H ODNP enhancements as a function of the applied MW input power. Three concentrations of TEMPOL in DI water are shown (sample volume always 130 nL). The error bars are based on an estimated relative error of 10 % for the corresponding thermal intensities. (c) Measured ^1H ODNP enhancement profile. A series of ODNP enhanced spectra, separately acquired within a ΔB -field range of ± 20 G, offset from the centre B_0 -field strength of 4940 G. Figure used with permission⁴⁰.

76 (note that typically $\Delta|f_L| > \Delta f_e$). MW frequency tuning is achieved, by introducing a thin strip of polyimide, featuring a gold
 77 coated tip, between the top and bottom glass substrate the MW resonators (maximal attainable tuning is $\Delta f_e \approx -0.55$ GHz). In
 78 fact, the gold patch creates an additional capacitive pathway for the high frequency signals, effecting both, frequency tuning
 79 and impedance matching. This method is very sensitive to the positioning of the gold coated tip of the tuner. As the effect is of
 80 capacitive nature, it is most pronounced at locations of high electric field strengths, primarily above the coupling gap region of
 81 the MW resonator, less so along the microstrip transmission line. As apparent from the Figure S3 (a), the change in frequency
 82 is unidirectional only, as the induced change in capacitance is positive (the capacitance is increased) the resonance frequency
 83 can only be lowered. The inset shown in Figure S3 (a) illustrates the influence of the tuners position on the amplitude of the S_{11}
 84 parameter is illustrated in the supplementary materials, indicating different degrees of impedance matching.

85 As stated above, the MW resonator as well as the RF resonator need to access the same sample volume. As a consequence
 86 two obvious but important requirements need to be fulfilled: (i) the EM performance of the MW resonator should not be
 87 compromised, once inserted into the RF coil, and closely related (ii) the RF performance of the NMR Tx/Rx coil should not
 88 be impaired by the presence of the MW resonator as well. For (i), the S_{11} measurements shown in Figure S3 (b) (bottom
 89 panel) prove that the MW resonance of the MW resonator is not spoiled once inserted into the RF coil assembly. This is
 90 achieved by two design choices, firstly both resonators are geometrically decoupled (fields orthogonal to each other) and
 91 secondly the aspect ratio of the conductors is very low, limiting the formation of eddy current substantially. Results on point
 92 (ii) are given further below. As described above, apart from the MW resonator's length parameter L , the geometry parameters
 93 constituting the coupling gap region are crucial and effects both the resonance frequency as well as the impedance matching.
 94 Figure S4 (a) shows the influence of the finger length C_1 on the resonance frequency f_i for a fixed, nominal coupling gap width
 95 of $C_{\text{gap}} = 25 \mu\text{m}$. Resonance frequencies and the loaded Q-factors $Q_L = f_0/(f_2 - f_1)$ were determined from the S_{11} curves
 96 measured by a calibrated network analyser. Measured values are compared to driven numerical EM simulations, with model
 97 properties as given in Table S1. Average measured (simulated) Q-factors are 33 (23) for the type 2 resonator. Assuming critical
 98 coupling ($\kappa = 1$) the unloaded measured Q-factors $Q_0 = Q_L(1 + \kappa)$ can be determined to be 66, which agrees reasonably well
 99 with the value of 75 as estimated (see supplementary material Section 1). However, most of the investigated MW resonators are
 100 under-coupled ($\kappa < 1$), suggesting the presence of unaccounted loss mechanisms due to, e.g., surface roughness, radiation loss
 101 and unknown high frequency dielectric losses of the involved materials.

102 ODNP enhanced ^1H NMR

103 The development of high performance double resonant structures, for *in situ*, resonant DNP probe heads, presents a central
 104 technical challenge. In the above subsection, one-port S-parameter measurements confirm, that (i) the EM performance of the
 105 MW resonator is not spoiled upon inserting the chip into the dedicated slot inside of the RF coil (see Figure 3). The above
 106 mentioned point (ii) is addressed by data shown in Figure S4 (b). The Figure compares the ^1H NMR spectra obtained by using
 107 a bare glass chip (no metallisation) with the spectrum acquired by using an actual metallised MW resonator chip. Except
 108 from a spectral shift, both spectra are identical, confirming, that the excitation/detection performance of the NMR coil is not
 109 impaired due to an inserted MW resonator chip. Following the measurement procedure given in the supplementary materials,
 110 a set of basic ^1H ODNP experiments was conducted. Figure 2 (a) compares the thermal (MW off) ^1H NMR signal to an

111 ODNP-enhanced spectrum (MW on), acquired from 130 nL of 10 mM TEMPOL dissolved in DI water. At this concentration,
112 the ODNP experiment shows a signal enhancement of $E \approx -54$ at a MW input power level of $P_{\text{MW}} \approx 0.52$ W (type 2 MW
113 resonator, $L = 3.635$ mm, $C_1 = 200$ μm , $C_{\text{gap}} = 20$ μm , $w_c = 100$ μm).

114 The NMR transmitter frequency was set to 20.96 MHz, using an RF input power of 2 W. A typical ODNP enhanced
115 ^1H spectrum features 0.7 ppm or 14 Hz FWHM line width spectral resolution with the shim system engaged. In order to
116 reduce undesired sample heating effects due to CW MW irradiation, the start-stop timing of the MW source was controlled by
117 TTL trigger signals of the NMR console. The inset in Figure 2 (a) shows a polarisation build-up curve as a series of ODNP
118 spectra acquired by successively increasing the MW irradiation time t_{rad} . The experiments were recorded using the same
119 type 2 MW resonator at a fix MW power of $P_{\text{MW}} = 130$ mW from a 15 mM TEMPOL DI water sample. In a post-processing
120 step a peak detection and fitting routine was applied to the data. Fitting the signal growth by employing the exponential
121 model $a[1 - \exp(-t_{\text{rad}}/\tau_{\text{MW}})]$, reveals a characteristic signal build-up time of $\tau_{\text{MW}} = 150$ ms. In order to establish steady state
122 conditions during each ODNP experiment, t_{rad} was typically set to between 200 ms to 800 ms.

123 Figure 2 (b) shows the ^1H signal enhancements $E(P_{\text{MW}})$ as a function of the applied MW input power, measured for three
124 radical concentrations. The NMR acquisitions were performed at a transmitter frequency of 21 MHz, a repetition delay of
125 3 s, an RF power of 2 W and a pulse length of 7 μs . The applied MW power levels, as set in unit decibel at the MW source,
126 were corrected for the employed attenuators and converted into unit watt. As apparent from the diagram (gray region), the
127 enhancements E deviate significantly from the expected fitting model, given by $1 - E = a_1 P_{\text{mw}} / (1 + a_2 P_{\text{mw}})$, for higher power
128 levels. This effect is due to the loss of sample, caused by dielectric heating for power levels exceeding 0.5 W. To fit the data,
129 only enhancements below 0.5 W were included. Figure 2 (c) shows an ODNP enhancement profile, whose envelope resembles
130 the EPR transitions of the ^{14}N radical.

131 Discussion and Conclusion

132 Due to the low polarisation field of 0.5 T, bare-bones 21 MHz NMR struggled to deliver a reasonable ^1H signal from the
133 130 nL small sample (containing 10 mM TEMPOL water solution) despite careful shimming, but Overhauser enhancement
134 by microwaves at 14 GHz ($P_{\text{MW}} = 0.5$ W) could boost the signal-to-noise ratio by 54 in around $\tau_{\text{MW}} = 0.15$ s to 0.5 s of
135 irradiation. This enhancement level observed for the present system is in reasonable agreement with work previously published
136 by Armstrong et al.^{31,41}, who obtained measured ^1H enhancements of around -50 to -70 from sample solutions containing
137 15 mM and ^{14}N 4-amino-TEMPO and ^{15}N 4-oxo-TEMPO employing similar MW power levels but an 0.35 T electromagnet.

138 The EPR frequency at 0.5 T was very close to the absorption line of water, so that extended power irradiation eventually
139 lead to heating of the sample, and evaporation, despite careful design of the resonator. This can be countered by operating the
140 measurement at a less absorptive EPR/DNP frequency, or by active cooling of the sample during measurement, for example
141 based on the Peltier effect.

142 The paper does not address the miniaturisation of the spectrometer, nor does it consider a compact solution for magnet
143 stabilisation. Recent work by Jouda⁴² has explored EPR detection utilising a commercial GHz source chip by Analog Devices
144 (e.g. ADF5610), and Anders et al.⁴³ have demonstrated a CMOS chip oscillator reaching 14 GHz that yields sufficient power
145 for the EPR excitation of a 200 μl sample, and enough sensitivity for detection. Very recently the Boero group⁴⁴ presented
146 a CMOS based single-chip DNP system for experiments inside an electromagnet. The authors conclude that employing
147 an all planar topology is limited in terms of NMR excitation homogeneity and confirm that the pronounced EM coupling
148 between the MW and RF resonant structures in their setup represents a major technical challenge. By suitable insulation and
149 power management based on available technologies, the feasibility of magnet thermal stabilisation is also not considered to be
150 technically demanding.

151 The compact probehead of this report was based on wafer scale microfluidic chip processing, precision multilayer PCB
152 manufacturing for the shim coils, combined with fused-deposition 3D printing for the holder and sweep coils, and was designed
153 to fit snugly into the commercial 0.5 T palm-top NMR magnet. The tight integration was especially facilitated by the high
154 degree of B_1 -field orthogonality between the microwave and radiofrequency resonators, thus suppressing coupling, nevertheless
155 did not compromise the system's scalability w.r.t. sample volume, or its modularity of separate functional components, such as
156 shims, sweep coils, resonators, and microfluidics.

157 The system's chemical shift resolution of 0.7 ppm compared favourably to the recent reports by Keller et al.³⁶ (0.3 ppm
158 using a hybrid magnet after active shimming) and Übrück et al.³⁷ (3.6 ppm ^1H NMR spectrum of acetic acid with passive
159 shims), whilst maintaining a high level of system compactness, and a low magnet weight.

160 This work thus clearly shows, for the first time, the feasibility of Overhauser DNP for a mass-producible microfluidic assay
161 in an ultra compact arrangement.

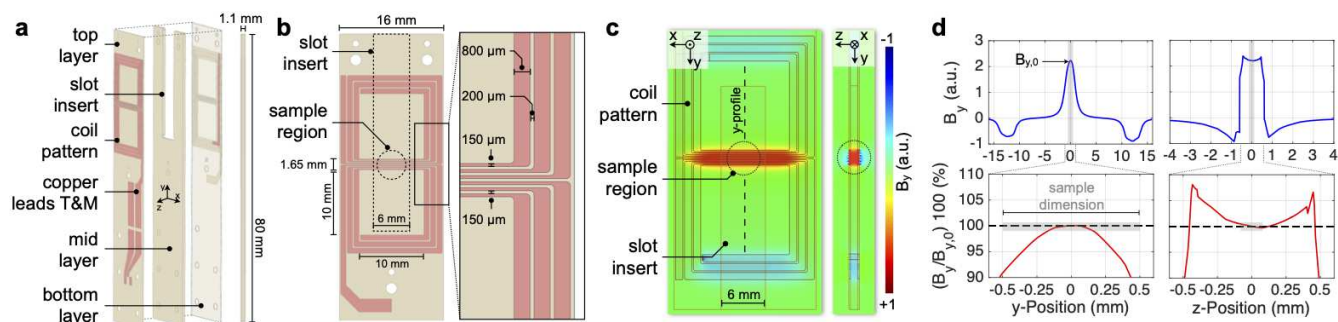


Figure 3. RF coil geometry and 3D electromagnetic (EM) field simulations at self-resonance (ca. 48 MHz). **(a)** Exploded view model of the stacked figure-8 coil. The total height of the pressed PCB stack is approximately 1.1 mm. A 6 mm × 30 mm sized slot is milled into the spacer mid layer (ca. 0.8 mm in height) to accept the fluidic insert featuring the MW resonator. **(b)** Zoomed-in details of the coil traces. The slot and sample region are indicated by dashed lines. **(c)** Density plot (top- and cross-sectional view) of the B_y -field component, showing three distinct high magnetic field regions due to in-phase field superposition. **(d)** B_y -field profiles along the y - ($x = z = 0$) and z -direction ($x = y = 0$) of the coil ($h_c = 1.2$ mm), as well as normalised data shown over the sample region (gray rectangles). Figure used with permission⁴⁰.

Materials and methods

System design

Figure 1 illustrates all major components of the ODNP probe head. The probe was formed from a stacked assembly, which inserted into a 0.5 T parallel-plate, permanent magnet. A figure-8 shaped, open topology Tx/Rx coil was used for RF excitation and NMR signal acquisition. A set of miniaturised bi-planar electrical shim coils reduced the B_0 -field inhomogeneities, as required for NMR spectroscopy. Nano-litre sized sample volumes were handled by a microfluidic chip that featured a co-integrated transmission line MW resonator to facilitate ODNP and EPR experiments. For phase sensitive EPR detection, a Helmholtz-type modulation coil was implemented. Our system design considerations addressed the following points:

Magnet effects. The concept accounts for typical characteristics of permanent magnets, such as low thermal polarisation, typically poor B_0 -field homogeneity, temperature induced B_0 -field drift, and limited space between the magnetic pole pieces.

EM-field effects. For an *in situ* ODNP system, the RF resonator, as well as the MW resonator, access the same sample volume, ideally without compromising performance. Therefore, the resonator topology allows sample excitation at both high (several GHz) and low (several MHz) frequencies, as needed for ODNP experiments. To minimise cross-talk, the MW-field direction is orthogonal to the direction of the RF-field, decoupling mutual inductive pathways.

Modularity. The ODNP probe permits a high level of integration while still remaining modular. The concept handles a sub-microliter sample volume and is envisioned to be scalable in dimension, allowing to adapt to diverse applications. The targeted design ultimately avoids manual manufacturing, and thus is producible by automated fabrication methods.

RF resonator

For NMR excitation and detection, a stacked layer coil topology was targeted. As sketched in Figure 3, the micro-inductor consisted of two vertically aligned coil traces of six turns each, resulting in an open volume coil geometry with a total number of 12 turns. The top and bottom coil patterns resemble the shape of two figure-eights, separated by a 800 μm thick spacer. Variable conductor trace widths reduce excessive eddy current losses^{45,46} and improve the quality factor of micro 2D inductors, here achieved by employing two track widths. The outer metal traces were chosen to be 800 μm; for the centre region the trace width was uniformly reduced by a factor of 5.3 to 150 μm. This served two purposes, (i) it concentrated all traces aligned with the y -axis within a ± 0.825 mm zone, overlapping the lateral dimension of the sample reservoir, and (ii) it increased the current density and hence B_y -field magnitude in that region.

As apparent from Figure 3 (b), a 6 mm × 30 mm slot was left open in the mid (spacer) layer of the stack in order to accommodate a microfluidic chip, featuring the MW resonator and sample reservoir. The RF excitation region was localised at the geometric centre of the figure-8 shaped coil pattern between the top and bottom planes. In this region, parallel coil traces guide currents in opposing direction on each face of the sample, resulting in a constructive B_1 -field superposition. Compared to a single layer coil design, the stacked approach offers several advantages, including a higher overall inductance, and improved B_1 -field homogeneity and magnitude, and low stray field components. The open coil topology accommodates the microfluidic chip, in a way that both RF and MW resonator are electromagnetically decoupled by their orthogonal geometric arrangement. The resonant coil's B_1 -field homogeneity at 48 MHz, as well as its electrical characteristics, were confirmed by finite-element

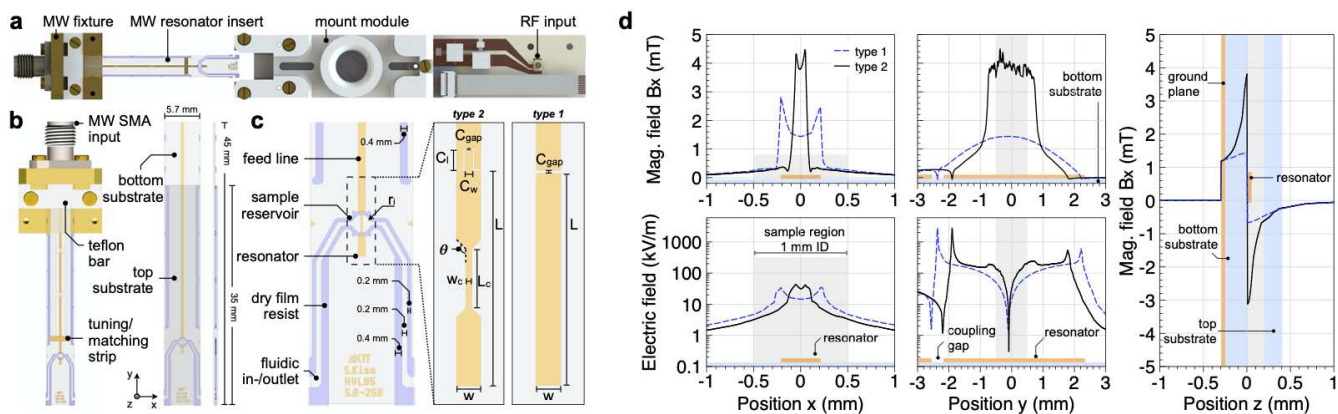


Figure 4. (a) Topview on the ODNP probehead model, shown with the MW resonator detached. (b) Overview of the MW fixture and the microfluidic chip. (c) Geometry details of the two designs of microstrip resonators (groundplane not shown). (d) Electric and magnetic field profiles as extracted from the EM simulations for resonator type 1 and 2. Profiles are shown along the corresponding axes. As guidance to the eyes, the metallisation of the resonator (depicted in orange) and sample dimensions (grey) are indicated in the diagrams. Figure used with permission⁴⁰.

EM field simulations, shown in Figure 3 (c) and (d).

The CAD model of the coil was imported into the simulation software (HFSS, version 16, ANSYS) as a sheet conductor implementing a finite conductivity boundary condition (copper). The coil was modelled inside a box-shaped air volume with an outer radiation absorption boundary. The structure was excited using a lumped port with a reference impedance of 50 Ω . The B_y -field density plot (Figure 3 (c)) reveals three distinct enhanced-field regions, caused by the in-phase field superposition at coil traces aligned along the x-direction, and a more than tripled B_y -field magnitude at the position of the sample reservoir. Figure 3 (d) also reveals the excellent B_y -field homogeneity $B_y/B_{y,0}$, with $B_{y,0} = B_y(x, y, z = 0)$. The geometry of the employed sample container is approximately a thin disc of low aspect ratio $\eta = d_z/d_x = 0.2$ (illustrated by gray regions within the diagrams). Therefore, inhomogeneities along the z-direction contribute a factor η less to the NMR spectral line broadening than those present along the x,y-directions.

MW resonator and microfluidic insert

For ODNP experiments, the electron spin transitions of radicals inside the sample are excited and ideally driven into saturation by means of MW radiation. Figure 4 (a) illustrates the ODNP probe head design and its microstrip line MW resonator integrated into a $(45 \times 5.7 \times 0.675) \text{ mm}^3$ ($1 \times w \times h$) microfluidic chip. In the figure, the MW resonator is shown detached from the RF coil. When inserted into the slot of the RF coil, the fixture is attached and held in place by the 3D-printed mounting module. The rectangular glass chips depicted in Figure 4 (b) are mechanically fixed and electrically connected onto a brass fixture. A Teflon bar provides electrical compression contact between the inner conductor of the SMA connector and the MW launch point of the transmission line. Figure 4 (c) shows geometrical details of the fluidic channels, as well as the transmission line MW resonator designs considered. Important layout parameters, such as the resonator width w , length L , as well as the coupling geometry, were analytically determined and served as a reasonable starting point for further EM simulations.

Two microstrip designs were investigated. Type 1 is a standard $\lambda/2$ -resonator. Type 2 is also a $\lambda/2$ -resonator, but featuring a symmetric constriction. To maintain alignment of the centre of the MW resonator to the centre of the B_1 -field of the RF coil, as well as the sample volume for B_0 -field shimming, the distance between the MW launch point of the microstrip feed line and the MW resonator's centre point ($L/2$) was kept fixed at 35 mm for all design variations. As a consequence, the length of the feed line varies for changing resonator lengths. The resonator is operated as a half-wavelength, open-circuited resonant strip of length L . The resonance frequency f_0 of the fundamental mode is primarily adjusted by the choice of L which, neglecting fringing effects, can be estimated by

$$L = m \frac{\lambda}{2} = m \frac{c}{2f_0 \sqrt{\epsilon_\ell}}, \quad (1)$$

with the guided wavelength λ , speed of light c , integer mode number $m = 1, 2, 3, \dots$, the effective dielectric permittivity ϵ_ℓ . For a targeted resonance frequency of 14 GHz ($m = 1$) and $\epsilon_\ell = 4.52$, the required length of an uncoupled resonator is approximately 5 mm. The width w of the resonator is chosen to be equal to the width of the feed line, whose characteristic impedance

226 $Z_0 = 50 \Omega$ is determined by known equations⁴⁵. For the employed borosilicate glass substrate of $h = 0.3$ mm in height, a
 227 characteristic impedance of 50Ω is met for the ratio of $w/h = 1.47$, which results in a track width of $w = 0.441$ mm. Table S2
 228 provides an overview of the involved geometry and material parameters. The supplementary materials present the detailed
 229 resonator design following standard electrical engineering procedures, as well as the characterisation using field simulations.

230 For electron paramagnetic resonance, an ideal-performing resonator topology should maximise the microwave conversion
 231 efficiency $\Lambda = B_{\text{MW}}/P^{1/2}$ that penetrates the sample, and should ensure EM field separation with low sample penetration
 232 of the electric field, to minimise dielectric sample heating. Polar and electrically conductive sample solutions, in particular,
 233 readily absorb MW power P_{abs} , which scales as $P_{\text{abs}} \propto \epsilon |E_{\text{MW}}|^2$, with ϵ being the sample permittivity, and can cause significant
 234 increases in temperature and sample evaporation. The field profiles shown in Figure 4 (d) illustrate this characteristic. High
 235 E-field magnitudes are present at the two opposite sites of the resonator, particularly across the capacitive coupling region. At
 236 resonance, the magnetic H_x -field maximum is found to be at the sample location, i.e., the resonator's centre.

In comparing the field profiles for both resonator types, Figure 4 (d) reveals significantly higher magnetic field peak values
 $H_{xy,\text{max}}$ for resonator type 2 (1.6 and 3.1 times higher than that for type 1 along the x and y axes). As expected, the geometric
 constriction of type 2 lead to high current densities and an increased magnetic field, covering a stripe across the 1 mm sample
 diameter. However, in absolute terms this came at the price of considerably higher E-field strengths (1.3 times higher along the
 x-axis, 2.7 times higher along the y-axis) penetrating the cylindrical sample region. From the EM simulation, the power to
 field conversion factor can be estimated to be $\Lambda_{\text{type 1}} \approx 2 \text{ mT W}^{-1/2}$ and $\Lambda_{\text{type 2}} \approx 4.5 \text{ mT W}^{-1/2}$. To quantify the performance
 indicators, the field energy ratio Γ around the sample region was determined from the profiles presented in Figure 4 (d), given
 as

$$\Gamma = \frac{\mu_0 \int H_x^2 ds}{\epsilon_0 \int E^2 ds}. \quad (2)$$

237 Interestingly, Γ for both resonators along the x- and y-axes are found to be remarkably similar (approximately $\Gamma_x = 2.6 \times 10^{14}$
 238 and $\Gamma_y = 1.0 \times 10^{14}$). The integration interval of the line integrals was placed symmetrically across the geometric centre of
 239 each resonator, with an upper and lower limit of plus/minus the sample diameter (± 0.5 mm). These results suggest that type 2
 240 resonators yield superior $H_{x,\text{max}}$ values, while offering similar performance to frustrate the electric field around their centre
 241 region, when compared to type 1 resonators. In other words, to achieve similar $H_{x,\text{max}}$ values, a type 1 resonator would require
 242 higher MW input power to match the values obtained by type 2. Alternatively, a reduced L of type 1 resonators might compensate
 243 for that disadvantage. However, this also would push the E-field maximum closer towards the sample region than is the case for
 244 the type 2 topology.

245 Permanent magnet

246 For ODNP experiments a palm-sized, parallel-plate type, 0.5 T NMR permanent magnet (PM-1055-050N, Metrolab Instruments
 247 SA, Switzerland) was used. The cylindrically shaped magnet had an outer diameter of 8 cm and featured an air gap between
 248 two NdFeB-poles, separated by approximately 11 mm, and thus defining the maximum height of the probe head assembly.
 249 B_0 -field adjustments, as well as field-sweeps, were accomplished via a built-in auxiliary coil, which provided an adjustment
 250 range of $\Delta B_{\text{aux}} = \pm 3.75$ mT, which translates into $\Delta f_e \approx \pm 98$ MHz and $\Delta f_{1\text{H}} \approx \pm 150$ kHz in terms of EPR and ^1H NMR
 251 frequencies, respectively. As shown in Figure 5 (a), the magnet was mounted inside a Faraday cage box, providing RF-shielding,
 252 as well as a thermally stable environment. For optimal NMR performance, the location of a region inside the magnet with
 253 minimal magnetic field gradient was determined from an accurate B_0 -field map using a Hall probe (DTM-151, Group 6, New
 254 Zealand) and an x/y-linear stage (VT-80, Physik Instrumente GmbH, Germany). To improve measurement reproducibility
 255 and to reduce thermally induced B_0 -field drift (-1200 ppm K^{-1} or a shift of about -24 kHz K^{-1} in ^1H Larmor frequency),
 256 a temperature-controlled fan heater was employed, raising the magnet's temperature stably above room temperature (see
 257 Figure S1).

258 Bi-planar shim coils

259 The NMR line broadening due to permanent magnet field inhomogeneity of several kHz are unacceptable when compared to
 260 spectrograms obtained from shimmed high field magnets (sub 1 Hz). NMR systems based on permanent magnets commonly
 261 require multiple electrical shim coils in order to restore homogeneity. In this work, a five channel bi-planar shim coil set was
 262 implemented that is based on a design originally proposed by W. E. Anderson⁴⁷ (implemented shim orders: x, y, z, z^2 , xy),
 263 placed between the magnet poles to correct for B_0 -field distortions. The shims were positioned 3 mm apart in the z-direction
 264 and covered a spherical shim region with a radius of approximately 1.5 mm. Figure 5 (c) shows the discrete shim coil track of a
 265 micro-fabricated shim PCB. Shims related to the x and y axes were implemented as rectangular coils, whereas the z and z^2
 266 shims used circular traces. Care was taken to adjust the geometry of each shim to account for its z-position within the multilayer
 267 PCB. Whenever possible, current return paths were routed to line up with the input current paths, in order to reduce undesired
 268 magnetic stray fields and noise-pickup effects.

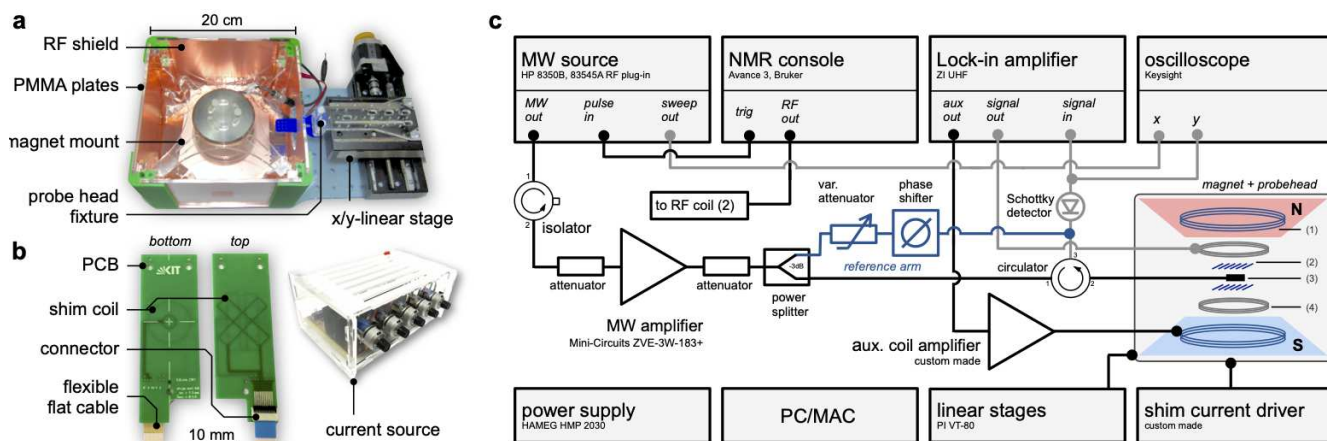


Figure 5. (a) The 0.5 T permanent magnet is suspended inside an RF-shielded box for environmental protection. For precise positioning, the probe is mounted on a motorised x/y linear stage. (b) Top and bottom of the fabricated PCB-based, five channel, bi-planar shim coils as well as the custom made shim current driver. (c) Schematic of the ODNP measurement setup. The reference arm (blue) as well as the one-port reflectometry setup (gray) are optional and were not permanently connected. Figure used with permission⁴⁰.

ODNP setup and signal processing

A block diagram of the EPR and NMR detection system is shown in Figure 5. The developed probe head was mounted on an x/y-linear stage (VT-80, Physik Instrumente GmbH, Germany) controlled by a PC and its position precisely maintained inside the magnet. The auxiliary signal output (± 10 V at 50Ω , $I_{\max} = 100$ mA) of a lock-in amplifier (UHFLI, Zurich Instruments, Switzerland) connected to the input of a custom built amplifier, which drove the magnet's auxiliary coil. The remainder of the measurement setup/procedure is standard and described in the supplementary materials.

Sample preparation and loading

A 100 mM 4-hydroxy-TEMPO (2,2,6,6-tetramethylpiperidyl-1-oxy, Sigma-Aldrich, $C_9H_{18}NO_2$, CAS number 2226-96-2, molecular weight $171.22 \text{ g mol}^{-1}$) stock solution, dissolved in non-degassed purified water was prepared and stored in a -20°C laboratory fridge. Working aliquots with concentrations of 1, 10 and 15 mM each were freshly prepared for measurements from the stock solution. For sample loading, a small amount of radical solution was pipetted onto a clean hydrophobic surface (Parafilm[®] 3M, laboratory film) forming an almost spherical droplet, which was carefully brought into contact with the inlet of the fluidic microchip. As shown in the inset of Figure 6 (a), the hydrophilic fluidic channels were rapidly filled by the aqueous sample solution via capillary force, without trapping any air bubbles. Reversible sealing of the in- and outlet of the chip was difficult and was simply omitted for most of the measurements. However, best sealing results were achieved by employing a droplet of wax. Due to the change in the dielectric environment of the microwave resonator upon sample loading, the resonator's resonance frequency is influenced. The change in frequency Δf_L depended on the sample properties and, for an aqueous sample solution, could be a shift of down to -300 MHz. For each resonator, the resonance frequency was fine-tuned (see tuning/matching strip) as close as possible to the electron frequency-equivalent of the magnet's static B_0 -field value (typically around 13.84 GHz).

Microfabrication

RF and shim coils

The stacked figure-8 NMR coil was realised as a high resolution PCB (PCB outline 80 mm by 16 mm, total thickness of ca. 1.1 mm), fabricated from high frequency, ultra-low loss laminates (R5775 Megtron 6, $\tan \delta = 0.004$ at 12 GHz, $\epsilon_r = 3.6$, $T_g \approx 185^\circ\text{C}$) in a 4 layer process. The tin coated copper tracks were $35 \mu\text{m}$ thick with a minimal feature size of $100 \mu\text{m}$. In order to accommodate the MW resonator chip, a similar-sized rectangular shape was cut out from the $800 \mu\text{m}$ core layer. For the RF connection, a low profile surface mount 50Ω micro coaxial connector (Molex, MCRF Series) was soldered to the PCB.

The five channel electrical shim set was realised as an 8-layer PCB, arranged in a bi-planar fashion. The multilayer stack comprised eight signal layers, each featuring $35 \mu\text{m}$ thick copper tracks, chemically coated by tin. The vertical space in the z-direction of the magnet was limited, necessitating the use of a compact 10 pin surface mount connector (Molex, Easy-On, FD19 Series) accepting a flat flexible cable to connect the coils to the current sources. In order to ensure the correct separation

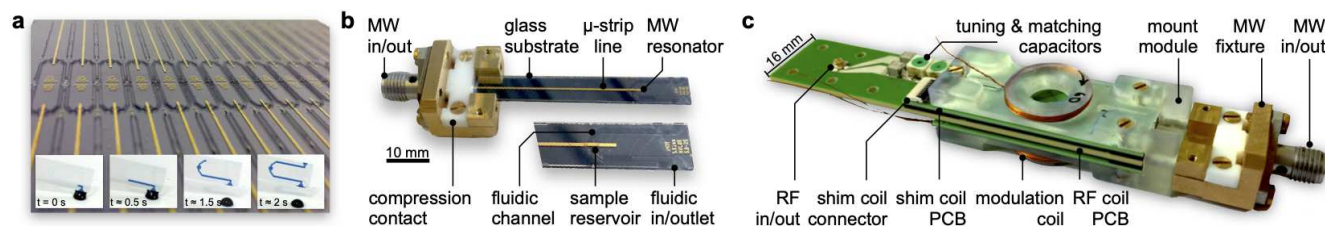


Figure 6. (a) Photograph of a bonded wafer stack featuring 30 individual microstrip resonators. The insets demonstrate the loading of aqueous sample (colored by blue pigments) via capillary forces. (b) Fabricated MW fixture, equipped with a resonator chip. (c) Fabricated ODNP probe head, shown with the MW insert being inserted into the stacked figure-8 NMR transceive coil. Figure used with permission⁴⁰.

300 in the z-direction, the shim PCBs were not directly attached to the RF coil PCB, but were suspended on each side (top and
 301 bottom) by a pair of spacers of defined height.

302 Microwave fixture

303 The MW fixture, as shown in Figure 6 (b) was precision milled from non-magnetic brass. A 50 Ω stainless steel RF connector
 304 (Part Nr. 1052902-1, TE Connectivity) was mounted on the front panel of the fixture. To avoid extensive MW signal loss
 305 and reflection effects, the microstrip signal launch region was designed so that (i) the ground return path was continuous and
 306 minimal and (ii) impedance mismatches were minimised⁴⁸. Addressing (i), the brass surface in contact with the microstrip
 307 ground plane was continuous and smooth, minimising surface resistance. For point (ii), the 50 Ω condition was maintained at
 308 the transitions between the connector and the fixture, as well as the connectors' signal pin and the microstrip. For solderless
 309 and flexible mounting of the resonators, a low-loss dielectric bar made from Teflon was used to provide an electrically reliable
 310 compression contact.

311 Microwave resonator

312 The microstrip line MW resonators were batch fabricated and defined by UV lithography (EVG[®] 620, Mask Alignment System,
 313 Austria). Square shaped (101 × 101) mm² borosilicate glass substrates (D 263[®] T eco, SCHOTT, tan δ = 0.01, ε_r = 6.3) of
 314 0.3 mm thickness were cleaned and coated on their top and bottom faces with a chromium and gold layer (10 nm Cr, 50 nm Au)
 315 by physical vapour deposition. The gold layer provided an electrically conductive seed layer for the following electroplating
 316 step. Dicing tape (Ultron systems, Minitron GmbH) was laminated to the substrate's bottom face for protection. A UV sensitive
 317 10 μm thick photoresist (SU-8 3005, MicroChem Corp.) was spin-coated and structured by UV light. Unexposed areas of the
 318 resist formed open windows after development and provided molds for the subsequent electroplating (Arauna, 25 g L⁻¹ Au) step,
 319 which was timed to reach a metal thickness of approximately 3 μm. The SU-8 resist mold was removed by means of a highly
 320 reactive plasma etching step (R3T STP 2020, Muegge GmbH, Germany), followed by cleaning the substrate in isopropanol,
 321 acetone, and deionised water. Wet-chemical etching of the gold seed layer in potassium iodide (KI/I₂) solution and chromium
 322 in a permanganate based etch solution (Cr-etch-200, MicroChemicals GmbH) revealed a clean glass surface in unplated areas.
 323 For the wet-chemical etching steps, the bottom side of the substrate was protected by unexposed, soft baked 4 μm thick resist
 324 (AZ4533, MicroChemicals GmbH), which was subsequently stripped. The average roughness of the gold metal structures
 325 was R_q ≈ 0.13 μm, as determined by white light interferometry measurements. Three sheets (nominal thickness per sheet:
 326 55 μm) of permanent dry film resist (Ordyl SY355, Elga Europe), yielding a total thickness of 165 μm were laminated to the top
 327 face of the substrate, using an office hot roll laminator (Photonex-Sync 235/325, GMP Co. Ltd., Korea) at a temperature of
 328 85 °C⁴⁹. The dry film resist served two purposes. Firstly, the fluidic channels and reservoirs were formed from it by means of
 329 UV lithography. Secondly it provided an adhesive bond interface for the top glass substrate. As reported in⁴⁹⁻⁵¹, the optimum
 330 dosage (180 mJ cm⁻¹ to 280 mJ cm⁻¹) for the UV exposure of the dry film resist, and bond temperature of (80 °C to 120 °C),
 331 were critical for the subsequent full wafer adhesive bond. However, as reported by Mueller et al.⁵² and in agreement with our
 332 experience, optimal post-exposure parameters were critical as well. A high bond yield was only achieved with dry film resist
 333 not fully cross-linked, thus still plastic and compliant enough to facilitate a firm bond with the glass substrate when subjected
 334 to heat (> T_g) and pressure. A 0.2 mm thick cover glass substrate (D 263[®]T eco, Schott) was bonded to the structured dry
 335 film resist by applying constant force and temperature to seal the chip, using a hot embossing tool (EVG510[®] HE, EV Group,
 336 Austria). The ODNP probe head assembly is pictured in Figure 6 (c).

Acknowledgements

SZK, NM, and JGK acknowledge financial support from the European Research Council (ERC) (contract number 290586). JGK acknowledges additional support from an EU2020 FET grant (TiSuMR, 737043), ERC-SyG (HiSCORE, 951459), the DFG under grant KO 1883/39-1 optiMUM, in the framework of the German Excellence Initiative under grant EXC 2082 "3D Matter Made to Order", and the KIT-VirtMat initiative "Virtual Materials Design II". NM and JGK acknowledge the partial financial support of the Helmholtz Association through the programmes "Science and Technology of Nanosystems - STN", and "BioInterfaces in Technology and Medicine - BIFTM". All Authors would like to acknowledge the support of the Karlsruhe Institute of Technology (KIT), providing the infrastructure to realise this work.

Conflict of interests

JGK declares his involvement as founder and shareholder of Voxalytic GmbH, a startup company that produces miniaturized NMR devices. The other authors declare that they have no conflict of interest.

Contributions

The idea conceptualization and system design was derived by SZK and JGK. SZK fabricated and optimised the experimental setup, carried out the system characterisation, performed the experiments, and conducted data analysis. NM and JGK supervised the work gave feedback throughout the project. SZK wrote the original draft of the manuscript. All authors contributed to the editing the final draft of the manuscript.

References

1. Zalesskiy, S. S., Danieli, E. & Blümich, B. Miniaturization of NMR systems: Desktop spectrometers, microcoil spectroscopy, and "NMR on a chip" for chemistry, biochemistry, and industry. *Chem. Rev.* **114**, 5641–5694 (2014).
2. Mitchell, J., Gladden, L. F., Chandrasekera, T. C. & Fordham, E. J. Low-field permanent magnets for industrial process and quality control. *Prog. Nucl. Magn. Reson. Spectrosc.* **76**, 1–60 (2014).
3. Lee, H., Sun, E., Ham, D. & Weissleder, R. Chip-NMR biosensor for detection and molecular analysis of cells. *Nat. Medicine* **14**, 869–874 (2008).
4. Ha, D., Paulsen, J., Sun, N., Song, Y.-Q. & Ham, D. Scalable NMR spectroscopy with semiconductor chips. *Proc. Natl. Acad. Sci. United States Am.* **111**, 11955–11960 (2014).
5. Anders, J., Handwerker, J., Ortmanns, M. & Boero, G. A low-power high-sensitivity single-chip receiver for NMR microscopy. *J. Magn. Reson.* **266**, 41–50 (2016).
6. Lei, K.-M. *et al.* A Handheld High-Sensitivity Micro-NMR CMOS Platform With B-Field Stabilization for Multi-Type Biological/Chemical Assays. *IEEE J. Solid-State Circuits* **52**, 284–297 (2017).
7. Gruschke, O. G. *et al.* Lab on a chip phased-array MR multi-platform analysis system. *Lab on a chip* **12**, 495–502 (2012).
8. Ryan, H., Smith, A. & Utz, M. Structural shimming for high-resolution nuclear magnetic resonance spectroscopy in lab-on-a-chip devices. *Lab on a chip* **14**, 1678–1685 (2014).
9. Massin, C. *et al.* Planar microcoil-based microfluidic NMR probes. *J. Magn. Reson.* **164**, 242–255 (2003).
10. Ehrmann, K. *et al.* Microfabrication of Helmholtz Coils with Integrated Channels for NMR Spectroscopy. In *19th IEEE International Conference on Micro Electro Mechanical Systems*, 366–369 (IEEE, 2006).
11. Ehrmann, K. *et al.* Microfabricated solenoids and Helmholtz coils for NMR spectroscopy of mammalian cells. *Chem. Commun.* **7**, 373 (2007).
12. van Bantum, P. J. M., Janssen, J. W. G., Kentgens, A. P. M., Bart, J. & Gardeniers, J. G. E. Stripline probes for nuclear magnetic resonance. *J. Magn. Reson.* **189**, 104–113 (2007).
13. Utz, M. & Landers, J. Magnetic Resonance and Microfluidics. *Science* **330**, 1056–1058 (2010).
14. Finch, G., Yilmaz, A. & Utz, M. An Optimised Detector For In-Situ High-Resolution NMR In Microfluidic Devices. *J. Magn. Reson.* (2015).
15. Meissner, M. V. *et al.* Ink-jet printing technology enables self-aligned mould patterning for electroplating in a single step. *J. Micromechanics Microengineering* **25**, 1–9 (2015).
16. Spengler, N. *et al.* Heteronuclear Micro-Helmholtz Coil Facilitates μm -Range Spatial and Sub-Hz Spectral Resolution NMR of nL-Volume Samples on Customisable Microfluidic Chips. *PLOS ONE* **11**, e0146384 (2016).

- 383 **17.** Davoodi, H. *et al.* An NMR-compatible microfluidic platform enabling in situ electrochemistry. *Lab on a chip* 3202–3212
384 (2020).
- 385 **18.** Raich, H. & Blümler, P. Design and construction of a dipolar Halbach array with a homogeneous field from identical bar
386 magnets: NMR Mandhalas. *Concepts Magn. Reson. Part B: Magn. Reson. Eng.* **23B**, 16–25 (2004).
- 387 **19.** Perlo, J. *et al.* High-Resolution NMR Spectroscopy with a Portable Single-Sided Sensor. *Science* **308**, 1279–1279 (2005).
- 388 **20.** Jachmann, R. C. *et al.* Multipole shimming of permanent magnets using harmonic corrector rings. *Rev. Sci. Instruments*
389 **78**, 035115 (2007).
- 390 **21.** Manz, B., Benecke, M. & Volke, F. A simple, small and low cost permanent magnet design to produce homogeneous
391 magnetic fields. *J. Magn. Reson.* **192**, 131–138 (2008).
- 392 **22.** Paulsen, J. L., Franck, J., Demas, V. & Bouchard, L. S. Least Squares Magnetic-Field Optimization for Portable Nuclear
393 Magnetic Resonance Magnet Design. *Magn. IEEE Transactions on* **44**, 4582–4590 (2008).
- 394 **23.** Parker, A. J., Zia, W., Rehorn, C. W. G. & Blümich, B. Shimming Halbach magnets utilizing genetic algorithms to profit
395 from material imperfections. *J. Magn. Reson.* **265**, 83–89 (2016).
- 396 **24.** Danieli, E., Perlo, J., Blümich, B. & Casanova, F. Small Magnets for Portable NMR Spectrometers. *Magn. Reson. Chem.*
397 **49**, 4133–4135 (2010).
- 398 **25.** Brideson, M. A., Forbes, L. K. & Crozier, S. Determining complicated winding patterns for shim coils using stream
399 functions and the target-field method. *Concepts Magn. Reson.* **14**, 9–18 (2002).
- 400 **26.** Terada, Y. *et al.* Magnetic field shimming of a permanent magnet using a combination of pieces of permanent magnets and
401 a single-channel shim coil for skeletal age assessment of children. *J. Magn. Reson.* **230**, 125–133 (2013).
- 402 **27.** Li, X., Hugon, C., Polesel-Maris, J., Martinez, V. & Sakellariou, D. Simple procedure for the fabrication of flexible NMR
403 shim coils. *Comptes Rendus Chimie* **16**, 967–971 (2013).
- 404 **28.** While, P. T., Meissner, M. V. & Korvink, J. G. Insertable biplanar gradient coils for magnetic resonance microscopy:
405 theoretical minimization of power dissipation for different fabrication methods. *Biomed. Phys. & Eng. Express* **4**, 035019
406 (2018).
- 407 **29.** Overhauser, A. Polarization of Nuclei in Metals. *Phys. Rev.* **92**, 411–415 (1953).
- 408 **30.** Carver, T. & Slichter, C. Polarization of Nuclear Spins in Metals. *Phys. Rev.* **92**, 212–213 (1953).
- 409 **31.** Armstrong, B. D. *et al.* Portable X-band system for solution state dynamic nuclear polarization. *J. Magn. Reson. (1969)*
410 **191**, 273–281 (2008).
- 411 **32.** Münnemann, K. *et al.* A Mobile DNP Polarizer for Clinical Applications. *Appl. Magn. Reson.* **34**, 321–330 (2008).
- 412 **33.** Garcia, S., Walton, J. H., Armstrong, B., Han, S. & McCarthy, M. J. L-band Overhauser dynamic nuclear polarization. *J.*
413 *Magn. Reson.* **203**, 138–143 (2010).
- 414 **34.** Neudert, O., Mattea, C., Spiess, H. W., Stapf, S. & Münnemann, K. A comparative study of ¹H and ¹⁹F Overhauser DNP
415 in fluorinated benzenes. *Phys. Chem. Chem. Phys.* **15**, 20717–20726 (2013).
- 416 **35.** Soltner, H. & Blümler, P. Dipolar Halbach magnet stacks made from identically shaped permanent magnets for magnetic
417 resonance. *Concepts Magn. Reson. Part A* **36A**, 211–222 (2010).
- 418 **36.** Keller, T. J., Laut, A. J., Sirigiri, J. & Maly, T. High-resolution Overhauser dynamic nuclear polarization enhanced proton
419 NMR spectroscopy at low magnetic fields. *J. Magn. Reson.* **313**, 106719 (2020).
- 420 **37.** Übrück, T., Adams, M., Granwehr, J. & Blümich, B. A compact X-Band ODNP spectrometer towards hyperpolarized
421 ¹H spectroscopy. *J. Magn. Reson.* **314**, 106724 (2020).
- 422 **38.** Johansson, B. A stripline resonator for ESR. *Rev. Sci. Instruments* **45**, 1445 (1974).
- 423 **39.** Narkowicz, R., Suter, D. & Stonies, R. Planar microresonators for EPR experiments. *J. Magn. Reson.* **175**, 275–284
424 (2005).
- 425 **40.** Kiss, S. Z. *Overhauser DNP probes for compact magnetic resonance*. Ph.D. thesis, Albert Ludwig University Freiburg,
426 Freiburg (2019).
- 427 **41.** Armstrong, B. D. & Han, S. Overhauser Dynamic Nuclear Polarization To Study Local Water Dynamics. *J. Am. Chem.*
428 *Soc.* **131**, 4641–4647 (2009).
- 429 **42.** Jouda, M. Private communication (2020).

- 430 **43.** Chu, A., Schlecker, B., Lips, K., Ortmanns, M. & Anders, J. An 8-channel 13 GHz ESR-on-a-Chip injection-locked
431 vco-array achieving 200 μM -concentration sensitivity. In *2018 IEEE International Solid - State Circuits Conference -*
432 *(ISSCC)*, 354–356 (2018).
- 433 **44.** Sahin Solmaz, N., Grisi, M., Matheoud, A. V., Gualco, G. & Boero, G. Single-Chip Dynamic Nuclear Polarization
434 Microsystem. *Anal. Chem.* **92**, 9782–9789 (2020).
- 435 **45.** Bahl, I. J. *Lumped Elements for RF and Microwave Circuits* (Artech House, 2003).
- 436 **46.** Lopez-Villegas, J. M., Samitier, J., Cane, C., Losantos, P. & Bausells, J. Improvement of the quality factor of RF integrated
437 inductors by layout optimization. *IEEE Transactions on Microw. Theory Tech.* **48**, 76–83 (2000).
- 438 **47.** Weston, A. A. Electrical Current Shims for Correcting Magnetic Fields. *Rev. Sci. Instruments* **32**, 241–250 (1961).
- 439 **48.** Coonrod, J. Signal Launch Methods for RF/Microwave PCBs. *Microw. J.* 1–5 (2014).
- 440 **49.** Vulto, P. *et al.* Microfluidic channel fabrication in dry film resist for production and prototyping of hybrid chips. *Lab on a*
441 *chip* **5**, 158–162 (2005).
- 442 **50.** Vulto, P., Huesgen, T., Albrecht, B. & Urban, G. A. A full-wafer fabrication process for glass microfluidic chips with
443 integrated electroplated electrodes by direct bonding of dry film resist. *J. Micromechanics Microengineering* **19**, 077001
444 (2009).
- 445 **51.** Huesgen, T. *et al.* Optimization and characterization of wafer-level adhesive bonding with patterned dry-film photoresist
446 for 3D MEMS integration. *Sensors Actuators A: Phys.* **162**, 137–144 (2010).
- 447 **52.** Müller, P. *Tunable optofluidic apertures*. Ph.D. thesis, freidok.uni-freiburg.de, Freiburg (2012).

Figures

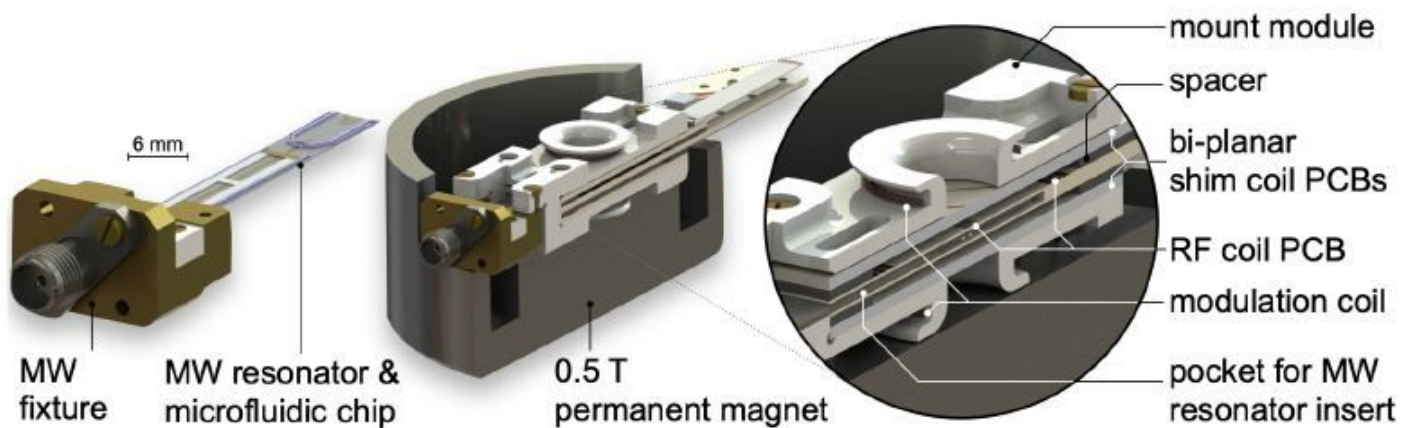


Figure 1

CAD views of the ODNP probe inside a palm-sized permanent magnet. The microfluidic chip features a sample reservoir and a MW resonator. A stacked figure-8 type RF transceive coil accepts the sample container and is sandwiched between a set of bi-planar electrical shim coils. A B₀-field modulation coil is part of phase sensitive EPR detection. Figure used with permission⁴⁰.

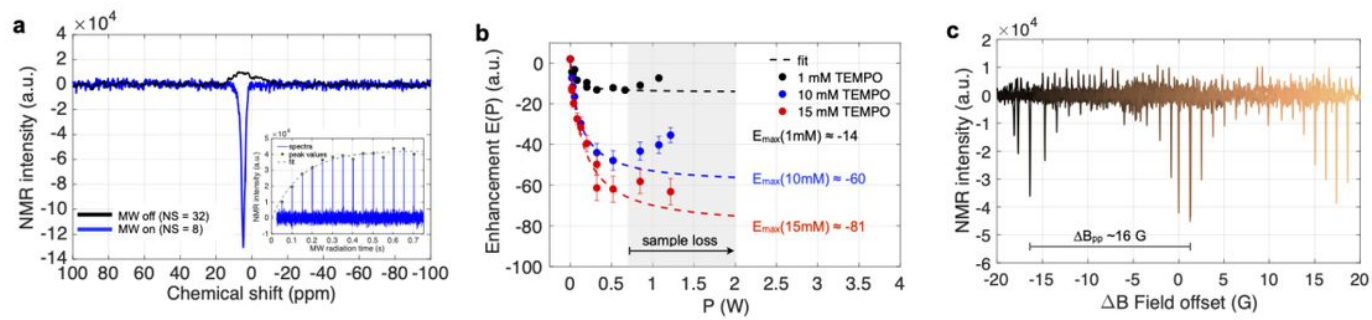


Figure 2

(a) Comparison between a thermal (32 scans) and the ODNP enhanced (8 scans) ¹H spectrum (130 nL of 10mM TEMPOL in DI water, PMW ≈ 0.52 W). The inset illustrates the build up of the ODNP signal as a function of MW radiation time (see text for details). (b) Measured ¹H ODNP enhancements as a function of the applied MW input power. Three concentrations of TEMPOL in DI water are shown (sample volume always 130 nL). The error bars are based on an estimated relative error of 10% for the corresponding thermal intensities. (c) Measured ¹H ODNP enhancement profile. A series of ODNP enhanced spectra, separately acquired within a DB-field range of ±20 G, offset from the centre B₀-field strength of 4940 G. Figure used with permission⁴⁰.

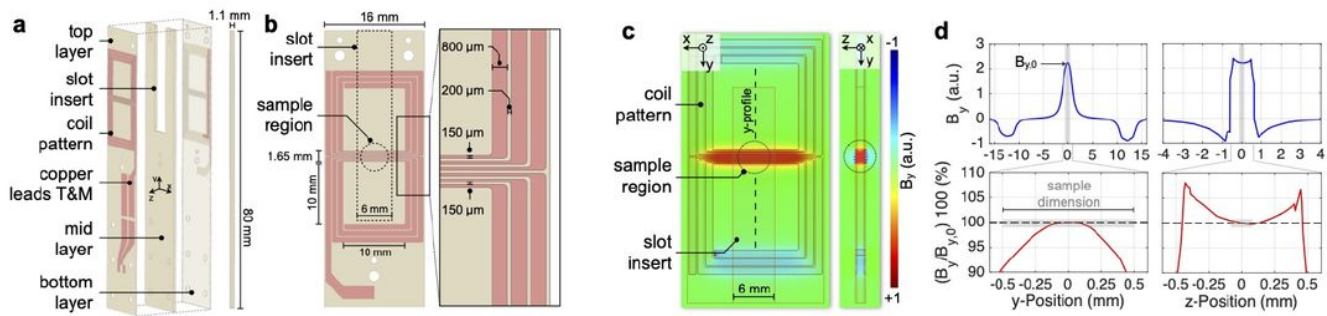


Figure 3

RF coil geometry and 3D electromagnetic (EM) field simulations at self-resonance (ca. 48 MHz). (a) Exploded view model of the stacked figure-8 coil. The total height of the pressed PCB stack is approximately 1.1 mm. A 6 mm \times 30 mm sized slot is milled into the spacer mid layer (ca. 0.8 mm in height) to accept the fluidic insert featuring the MW resonator. (b) Zoomed-in details of the coil traces. The slot and sample region are indicated by dashed lines. (c) Density plot (top- and cross-sectional view) of the B_y -field component, showing three distinct high magnetic field regions due to in-phase field superposition. (d) B_y -field profiles along the y - ($x = z = 0$) and z -direction ($x = y = 0$) of the coil ($h_c = 1.2$ mm), as well as normalised data shown over the sample region (gray rectangles). Figure used with permission40.

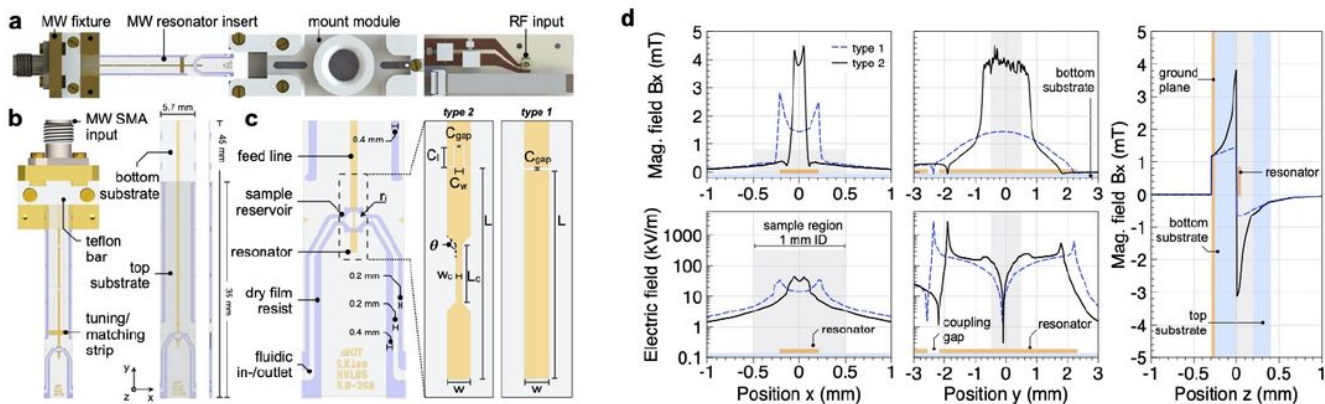


Figure 4

(a) Topview on the ODN probehead model, shown with the MW resonator detached. (b) Overview of the MW fixture and the microfluidic chip. (c) Geometry details of the two designs of microstrip resonators (groundplane not shown). (d) Electric and magnetic field profiles as extracted from the EM simulations for resonator type 1 and 2. Profiles are shown along the corresponding axes. As guidance to the eyes, the metallisation of the resonator (depicted in orange) and sample dimensions (grey) are indicated in the diagrams. Figure used with permission40.

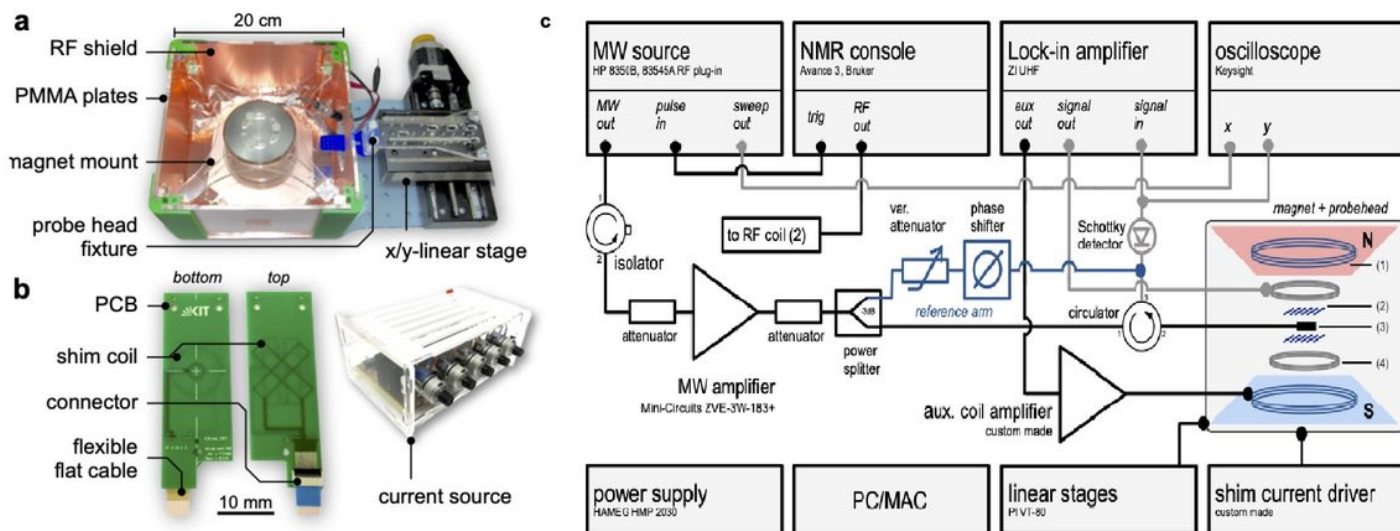


Figure 5

(a) The 0.5 T permanent magnet is suspended inside an RF-shielded box for environmental protection. For precise positioning, the probe is mounted on a motorised x/y linear stage. (b) Top and bottom of the fabricated PCB-based, five channel, bi-planar shim coils as well as the custom made shim current driver. (c) Schematic of the ODNP measurement setup. The reference arm (blue) as well as the one-port reflectometry setup (gray) are optional and were not permanently connected. Figure used with permission⁴⁰.

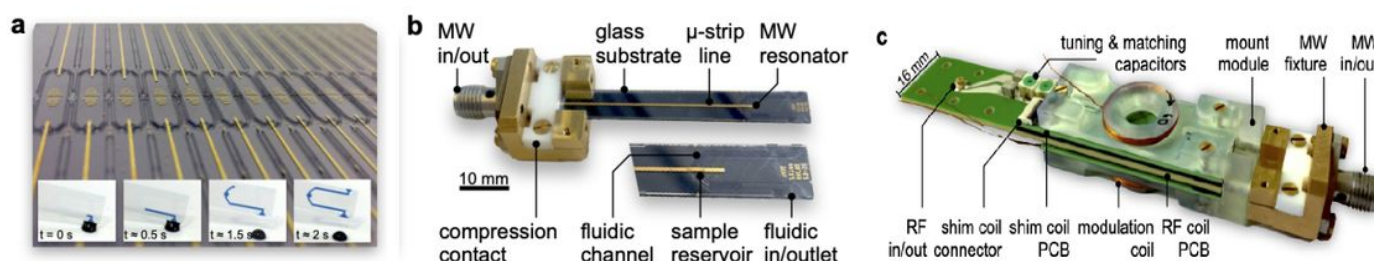


Figure 6

(a) Photograph of a bonded wafer stack featuring 30 individual microstrip resonators. The insets demonstrate the loading of aqueous sample (colored by blue pigments) via capillary forces. (b) Fabricated MW fixture, equipped with a resonator chip. (c) Fabricated ODNP probe head, shown with the MW insert being inserted into the stacked figure-8 NMR transceive coil. Figure used with permission⁴⁰.

Supplementary Files

This is a list of supplementary files associated with this preprint. Click to download.

- [ODNPScientificReportSuppInfo.pdf](#)